ANDRZEJ TEJCHMAN, JACEK TEJCHMAN

Scale effect in pile model tests

1. Introduction

The behaviour of piles under vertical load is one of the most complicated problems in soil mechanics, still being the topic of a number of model and in situ investigations or theoretical considerations. This is due to the fact that many phenomena occuring in the course of load transfering from pile into soil remain unexplained by existing theories. It particularly refers to interaction between pile shaft and soil. Shaft resistance of pile depends on a number of factors, among others on the displacements of the soil at the pile shaft in radial (horizontal) and axial (vertical) directions. Depending on the type of pile, way of its installation, loading direction (compression, tension) the effective normal (horizontal) stresses at the pile shaft can vary among the active and passive limit.

Very important problem in the analysis of the shaft resistance is dilatancy phenomena in a shear zone along the pile affecting the magnitude of skin friction. During loading of pile, a thin shear zone of soil along pile shaft is formed where soil dilates. The thickness of shear zone depends on roughness of pile surface, soil grains diameter, soil compaction and the boundary conditions of the whole system. The dilatancy is constrained by the mass of the surrounding soil, which causes additional increase of normal stresses. The dilatancy constraint causes thus a scale effect. As it is observed in the tests, the smaller piles for the same soil produced larger values of unit skin resistance and lateral effective stresses. The bigger pile model, the smaller the influence of dilatancy constraint on the stresses. Generally scale makes difficulty in the interpretation and transfering of the model test results directly on to fullscale (real conditions). The investigation of the shear zone thickness and the scale effects is not possible with

*Prof. Dr Eng. A. TEJCHMAN, Dr Eng. J. TEJCHMAN, Technical University of Gdańsk Poland

the aid of many constitutive laws which were laid down in the frame of nonpolar (classical) continuum, because they do not have any characteristic length. Therefore it is suitable to use another approach for description the behaviour of pile in soil. We made use of a Cosserat approach proposed by Mühlhaus (1987) which enables to describe the localization of deformation in granular material (shear zones) and the behaviour of granular particles by taking into consideration not only slip but also rotation among individual grains. The characteristic length in the Mühlhaus law is expressed by the mean grain size.

The aim of this paper is to analyse unit shaft resistance and the scale effect in model tests of pile in the cohesionless soil using finite element method and the Cosserat approach, what is novel in such investigations.

First a general review of pile investigations and obtained different relationship on the basis of Tejchman's model and full scale tests confirmed by many others researches is presented. Next basic principles of the use of finite element method and Cosserat approach for the analysis of pile bearing capacity (shaft resistance) is described. The examples of numerical calculations are given and comparison of these results with the results of performed model tests is discussed.

2. Analysis of load transfer from pile into soil

In the following figures the relationships concerning the load transfer from pile into non-cohesive soil are presented on the basis of own model and field tests (carried out by A. Tejchman). These results are confirmed by numerous aliens researches.

In Fig. 1 a general dependence of unit shaft resistance on pile diameter D for compression and tension pile is presented. A distinct scale effect is observed for model piles, particularly for compression loading and compacted soil. For piles with diameter $D > 30$ cm the dependence on D is relatively small, for larger diameter can slightly increase or decrease. Fig. 2, 3 and 4 show additionally some real results from model tests (Gwizdała 1977, Wernick 1978) and from field investigation (Spang 1972).

The dependence of unit shaft resistance τ_m on pile penetration depth is shown in Fig. 5. As it is known the values of τ_m^c increase nonlinearly with increase of depth and tends to constant value below so called critical depth. The value of τ_m^t for tension piles is practically constant, independent on depth.

In the investigations and in the practice, a significant differences between shaft resistance of pile in compression and in tension are observed. In Fig. 6 such relationship is shown. This fact is caused by different state of earth pressure for both cases, what is illustrated in Fig. 7 by means of K coefficient.

As a supplement concerning the analysis of pile behaviour, in the Fig. 8, the dependence of unit base resistance σ_p of pile diameter is presented. With increasing of pile diameter D, the decreasing of σ_p is observed. Fig. 9 shows values of σ_p for different D obtained from model tests by Gwizdała (1977), Fig. 10 from field tests by Spang (1972).
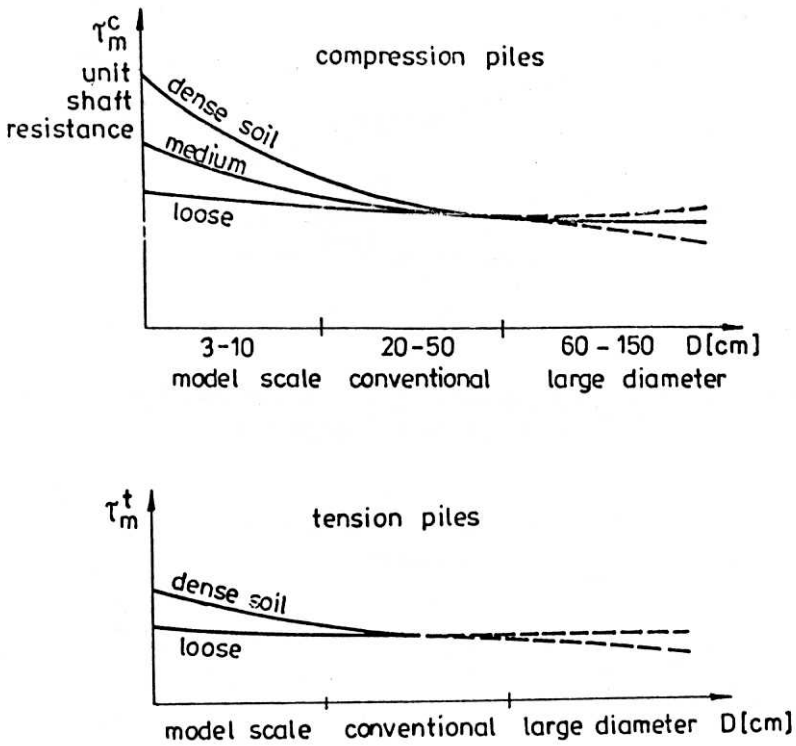
Fig. 1. General dependence of unit shaft mantle resistance τ_m^c (compression) and τ_m^t (tension) on pile diameter D
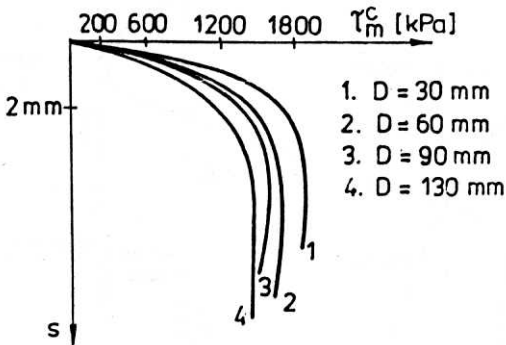

Fig. 2. Results of unit shaft resistance τ_m^c from model tests depending on pile diameter D
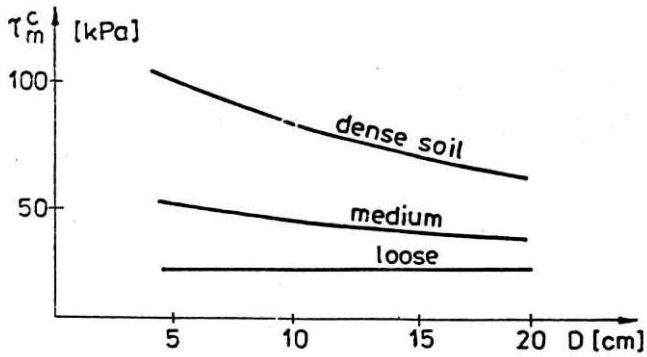
Fig. 3. Results of unit shaft resistance τ_m^c from model tests depending on pile diameter D and soil compaction
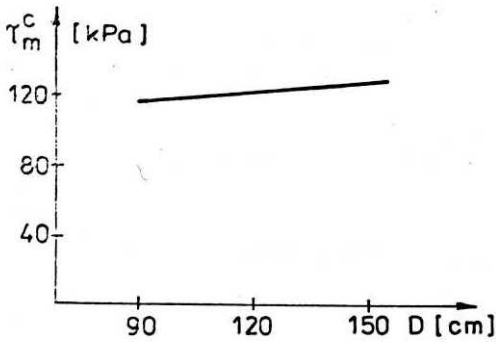

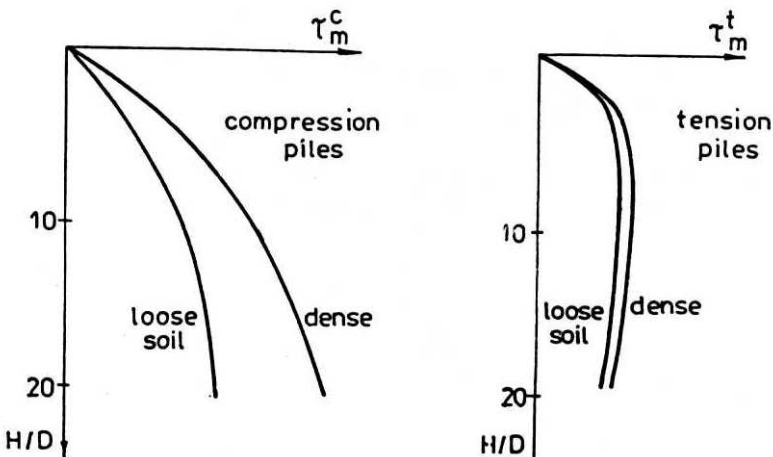Fig. 4. Results of unit shaft resistance τ_m^c from field tests depending on pile diameter D

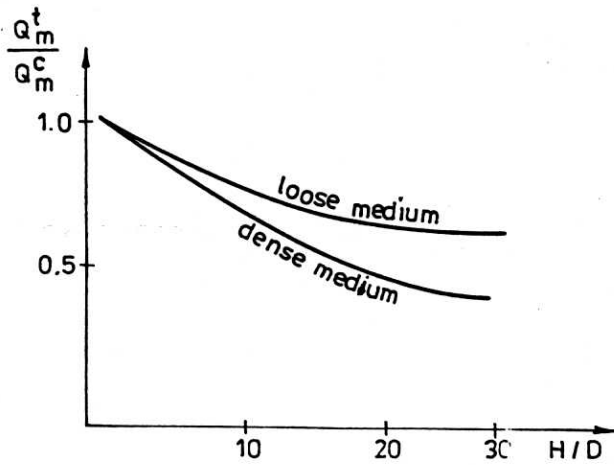Fig. 5. General dependence of unit shaft resistance on pile penetration depth

Fig. 6. Relationship between shaft resistance of pile in compression Q_m^c and in tension Q_m^t depending on relative penetration depth
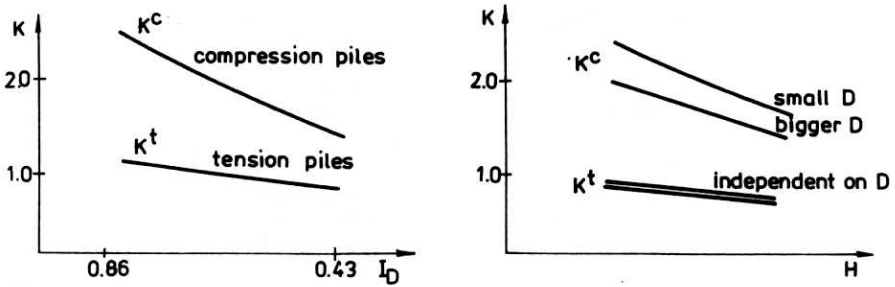

Fig. 7. Differences between coefficient of earth pressure K for compression and tension piles
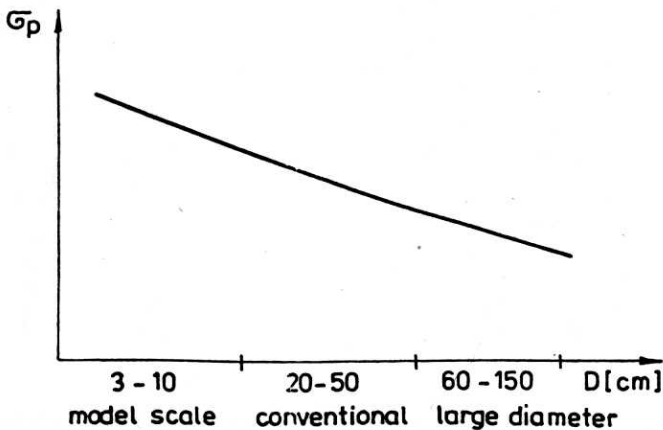

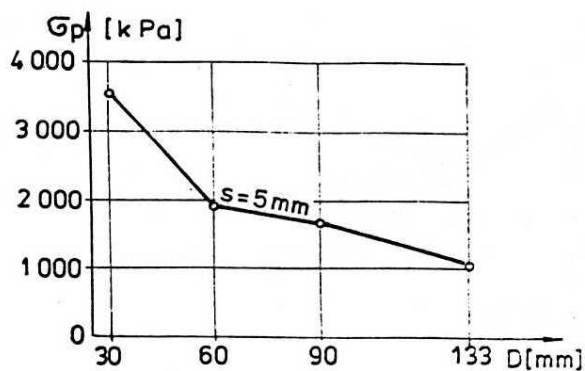Fig. 8. General dependences of unit base point resistance σ_p on pile diameter D

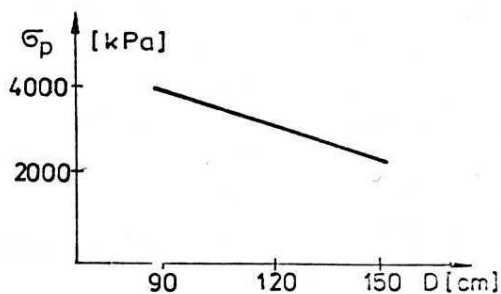Fig. 9. Model test results of dependences of unit base resistance σ_p on pile diameter

Fig. 10. Field test results of dependences of unit base resistance σ_p on pile diameter
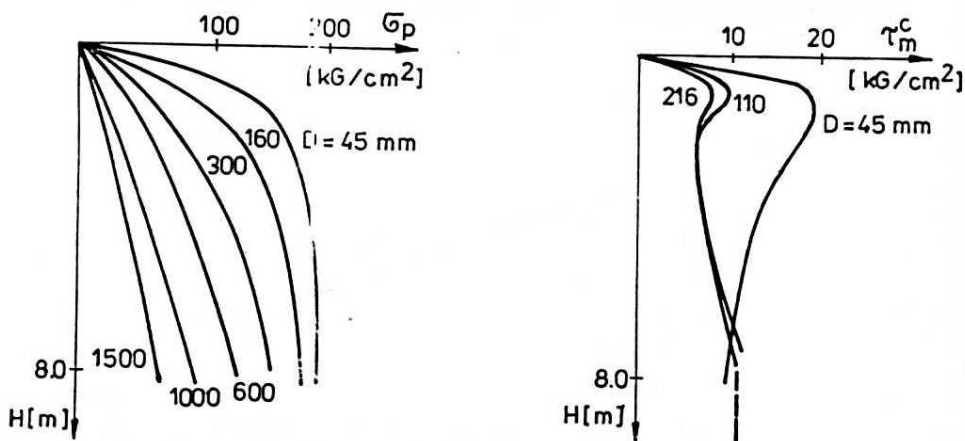

Fig. 11. Investigations of dependences of unit base resistance and shaft friction on pile diameter D carried out by Kérisel

At the end of this short illustrated review of pile behaviour in the soil is worth to remember the classical investigation results after Kérisel (1962), which demonstrate also clearly scale effects (Fig. 11).

3. Description and model test results

Some of the model test results are presented here to compare with numerical calculations, carried out on the basis of assumed Cosserat approach. The tests were carried out in dry uniform sand ($d_{50} = 0.24$ mm). The model set-up consisted of the following main elements: sand container $100 \times 100 \times 100$ cm, sand laying machinery, steel frame with loading arrangement and tracks on which sand laying machinery and main frame could be moved. Depending on the heights of fall for the sand the following four relative densities were obtained:

Table 1

	I_D	e	γ [kN/m^3]	ϕ (triaxial tests)
1	0.430	0.705	15.54	31.2°
2	0.595	0.646	16.09	33.2°
3	0.740	0.594	16.62	35.7°
4	0.865	0.549	17.10	38.8°

I_D – density index
e – void ratio
γ – unit weight
ϕ – angle of internal friction

The pile model was a brass pipe with an outer diameter of 50 mm and a total length of 850 mm. Sand was glued to the outer pile surface to provide a roughness. The essential part of the model was the cell containing strain gauges placed at the pile base to measure point load, and the mechanical dynamometer mounted on the pile top to measure total load on the pile. Hence it was possible to distribute the total load into point and shaft resistances. Pile model was pressed-in sand to a depth of 50 cm and then loaded to failure. As well as compression and tension tests were performed. An example of load-settlement curve obtained from test illustrates Fig. 12 (dense sand).

Since the comparative calculations were carried out only for one relative density of sand, below are listed (Table 2) only ultimate forces for $I_D = 0.865$ (as mean value from three experiments), Tejchman A. (1971).
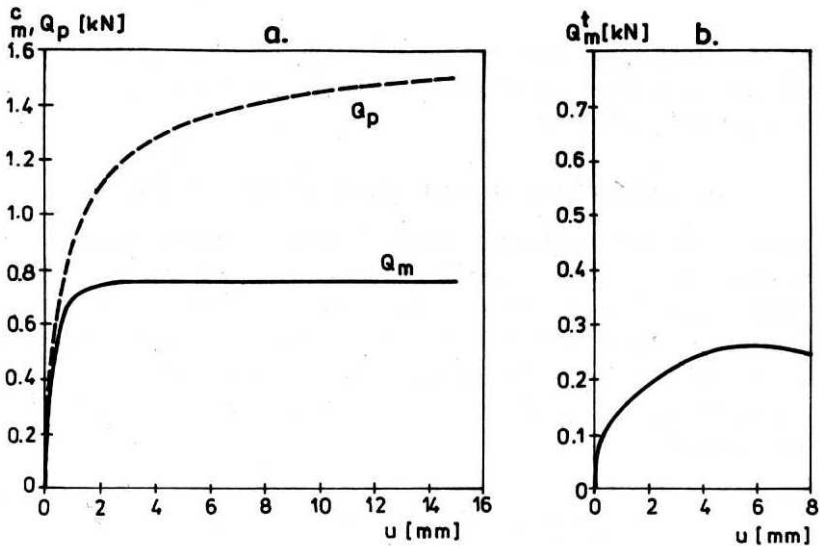
Fig. 12. Load-settlement curve from loading test (an example from model tests)
a) pushing in, b) pulling out

Table 2

H	I_d	e	compression pile					tension pile	
			Q_t^c	Q_p^c	p	Q_m^c	τ_m^c	Q_m^t	τ_m^t
cm			kN	kN	kPa	kN	kPa	kN	kPa
50	0.865	0.550	2.221	1.476	9.512	0.745	9.512	0.253	3.236

Q_t^c – ultimate total bearing capacity of pile (in compression)
Q_p^c – ultimate point resistance (in compression)
Q_m^c – ultimate mantle resistance (in compression)
Q_m^t – ultimate mantle resistance (in tension)
τ_m^c – ultimate unit mantle resistance (in compression)
τ_m^t – ultimate unit mantle resistance (in tension)

Additionally, to present a scale effect in model tests, the results of tests of precast concrete pile models are given. The models had cross-section of 35 × 35 mm and 50 × 50 mm and total length 120 cm. Piles were pressed in sand to the depth of 50 cm and 100 cm and next subjected to loading tests. Total load was measured by means of mechanical dynamometer, point resistance by means of strain gauges mounted at the pile base.

The model set-up consisted of concrete ring of 100 cm diameter and 150 cm height and loading arrangement. The sand used in the experiments had the following parameters (after placing in the sand container):

$$\gamma = 15.9 \text{ kN/m}^3, \quad \phi = 35°, \quad I_D = 0.50, \quad d_{50} = 0.23 \text{ mm}.$$

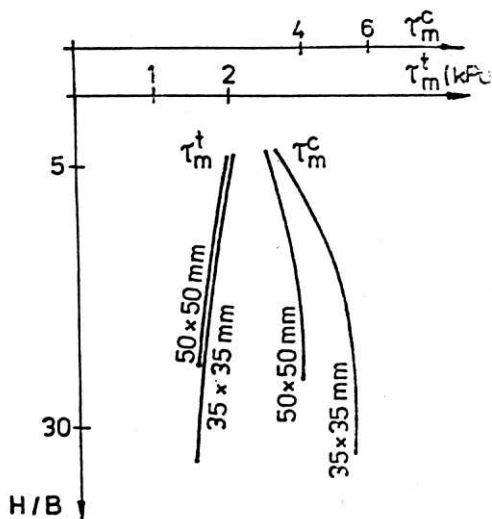The example of test results is listed in the Table 3 and shown in Fig. 13.

Fig. 13. Model test results of τ_m^c and τ_c^t for different pile cross-section

Table 3

B	H	compression pile		tension pile	
		Q_m^c	τ_m^c	Q_m^t	τ_m^t
cm	cm	kN	kPa	kN	kPa
3.5	50	0.702	5.786	0.123	1.961
5.0	50	0.363	3.628	0.206	2.059
3.5	100	0.834	5.884	0.206	1.471
5.0	100	0.853	4.217	0.343	1.667

B – width of pile model
H – penetration depth

4. A Cosserat model for granular bodies

4.1. Statics and kinematics (polar continuum, axi-symmetric case)

We use a Cartesian coordinate system x_1, x_2, in which the coordinates x_1, x_2 of each material point P relate to the actual configuration (Fig. 14). A local coordinate system is associated with each point P. During deformation each local coordinate system is displaced by the translations v_1 (radial translation), v_2 (vertical translation) and rotated by the angle ω. The rotation ω, which is independant of the translations v_1, v_2, will be marked with index c to distinguish it from the nonpolar rotation

$$\omega = \frac{1}{2}(v_{2,1} - v_{1,2}),\tag{1}$$

which results only from the displacement field v_1, v_2.
The kinematics are described in the frame of linear theory by the following quantities (all terms of second and higher order for $v_{i,j}$ and $\omega_{,i}$ are neglected):
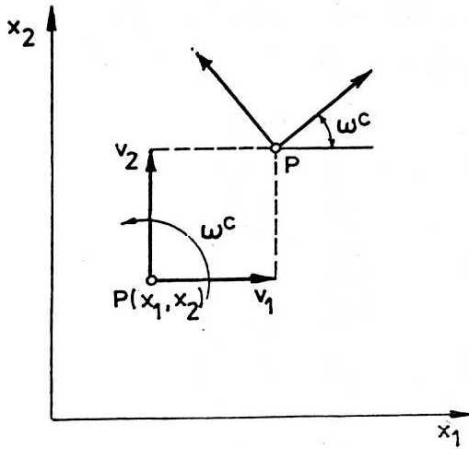
Fig. 14. Degrees of freedom in a Cosserat-continuum

$$\epsilon_{11} = v_{1,1}, \qquad \epsilon_{22} = v_{2,2} \tag{2}$$

$$\epsilon_{12} = v_{1,2} + \omega^c, \qquad \epsilon_{21} = v_{2,1} - \omega^c \tag{3}$$

$$\epsilon_{33} = \frac{v_1}{x_1} \tag{4}$$

$$\kappa_1 = \omega^c_{,1}, \qquad \kappa_2 = \omega^c_{,2} \tag{5}$$

where $(\ )_{,i}$ denotes $\partial(\ )/\partial x$, ϵ_{ij} the strain tensor, κ_i the curvature components and x_1 the distance of the material point from the symmetry axis.

The curvature tensor is a measure of the relative rotation of neighbouring coordinate systems, see Fig. 15 (analogy to beam bending theory). The quantities $\epsilon_{12}, \epsilon_{21}$ describe the relative deformations between displacement gradients $v_{1,2}, v_{2,1}$ and rotating local coordinate systems (Fig. 16). Owing to the presence of ω^c, $\epsilon_{12} \neq \epsilon_{21}$ in contrast to the nonpolar continuum. The nonsymmetric tensor ϵ_{ij} can be decomposed into a symmetric part with ϵ^s_{ij}

$$\epsilon^s_{11} = v_{1,1}, \quad \epsilon^s_{22} = v_{2,2}, \quad \epsilon^s_{33} = \frac{v_1}{x_1} \tag{6}$$

$$\epsilon^s_{12} = \epsilon^s_{21} = \frac{1}{2}(\epsilon_{12} + \epsilon_{21}) = \frac{1}{2}(v_{1,2} + v_{2,1}) \tag{7}$$

and into an antisymmetric part ϵ^a_{ij}

$$\epsilon^a_{11} = \epsilon^a_{22} = \epsilon^a_{33} = 0 \tag{8}$$

$$\epsilon^a_{12} = -\epsilon^a_{21} = \frac{1}{2}(\epsilon_{12} - \epsilon_{21}) = \omega^c - \frac{1}{2}(v_{2,1} - v_{1,2}) \tag{9}$$
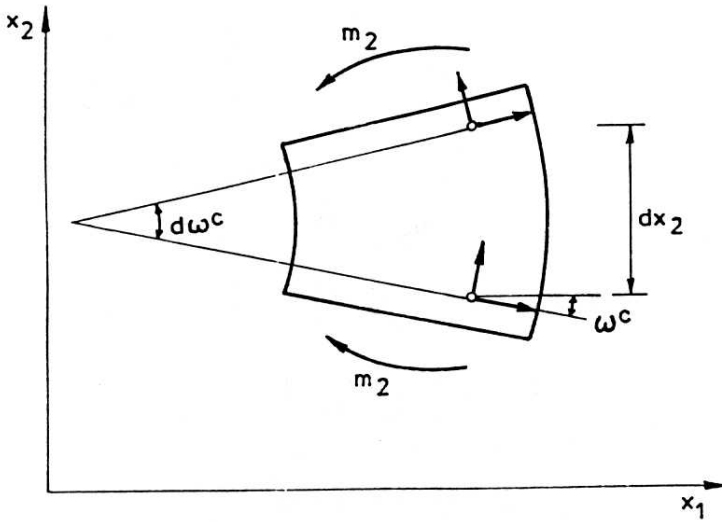
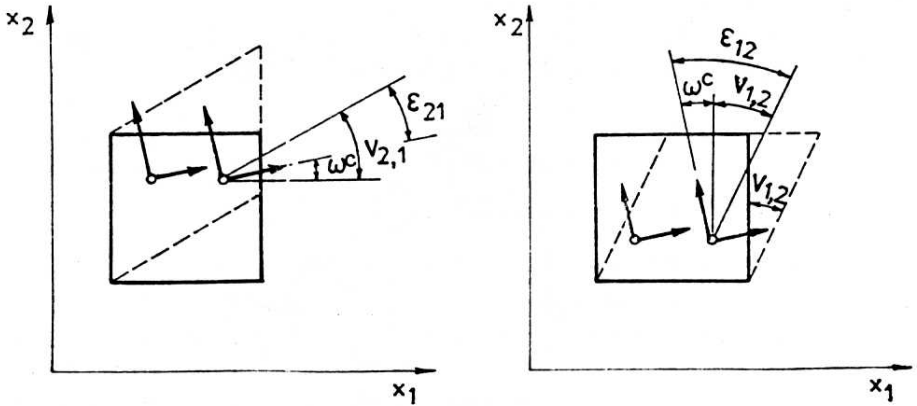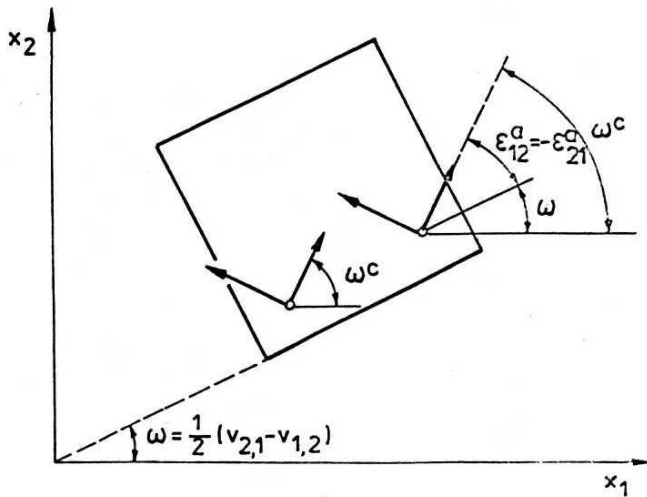Fig. 15. Deformation κ_2 and accompanying couple stress

Fig. 16. Deformations $\epsilon_{12}, \epsilon_{21}$

Fig. 17. Deformations ϵ_{12}^a, ϵ_{21}^a

The quantities ϵ_{11}^s, ϵ_{22}^s, ϵ_{33}^s, ϵ_{12}^s, ϵ_{21}^s describe a part of deformations which come only the nonpolar displacement field v_1, v_2. ϵ_{12}^a, ϵ_{21}^a describe the relative rotation of the local coordinate systems in regard to the mean rotation ω caused by the displacements v_1, v_2 (Eq. 1) – Fig. 17. In Cosserat-continuum there exist two different rotations, namely: nonpolar rotation ω (Eq. 1) and polar rotation ω^c. The stress tensor is in general nonsymmetric because of nonsymmetry of the deformation tensor ϵ_{ij}. It can be described by the five components of the nonsymmetric tensor σ_{ij} and two couple stresses m_i associated with the tensor κ_i.

The equilibrium equations of the seven Cosserat stresses for the static problem (Fig. 18) with the absence of the body couples read as follows
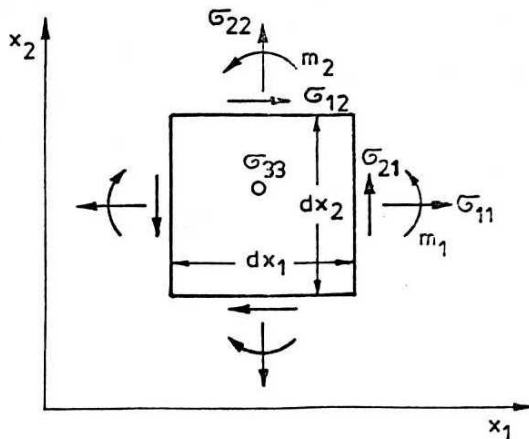

Fig. 18. Streses and couple stresses in a Cosserat continuum

$$\sigma_{11,1} + \sigma_{12,2} + \frac{1}{x_1}(\sigma_{11} - \sigma_{33}) = 0 \tag{10}$$

$$\sigma_{21,1} + \sigma_{22,2} + \frac{1}{x_1}\sigma_{21} = \gamma \tag{11}$$

$$m_{1,1} + m_{2,2} + \sigma_{21} - \sigma_{12} = 0 \tag{12}$$

where γ is the density of the material.

The virtual work δA per unit volume in a Cosserat continuum for any $\delta\epsilon_{ij}$ and $\delta\kappa_i$ is

$$\delta A = \sigma_{ij}\delta\epsilon_{ij} + m_i\delta\kappa_i \tag{13}$$

The couple stresses m_i can appear in granular materials because of eccentricity of contact forces against the centre of gravity of the grains. Their presence may be also explained as follows. Consider a square element (l_1, l_2) of a nonpolar continuum (Fig. 19), where σ_{12} and σ_{21} are the average value of shear stresses along the sides l_1 and l_2 of the element. The normal stresses σ_{11} and σ_{22} at the sides are assumed to be variable in the 1- and 2-direction. On the basis of equilibrium equations, the stresses σ_{11} and σ_{22}
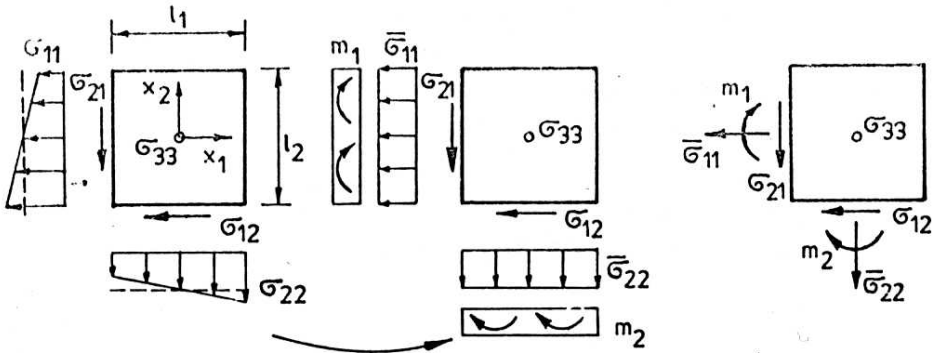

Fig. 19. Stresses at an element in nonpolar continuum

are statically equivalent to a force and a moment or to a force intensity (stress) and a moment intensity (couple stress).

To summarize, a Cosserat continuum differs from a nonpolar continuum through the fact that the rotation ω^c appears in the deformation field which is independant of the translations. Owing to that, each material point has three degrees of freedom of a rigid body. The rotation ω^c causes the curvatures κ_i which are associated with the couple stresses m_i. As a result, the deformation tensor ϵ_{ij} and the stress tensor σ_{ij} are nonsymmetric. For more details about the polar continuum the readers are refered to Günther (1958), Schäfer (1967), Mindlin (1969).

5. Constitutive relation for granular materials

An elasto-plastic consitutive law with isotropic hardening and softening in the frame of a Cosserat-continuum was laid down first by Mühlhaus (1987). His law differs from an usual theory of plasticity by the presence of the couple stresses and the mean grain diameter.

The following form is used:

$$\epsilon_{ij} = \epsilon_{ij}^e + \epsilon_{ij}^p, \quad \kappa_i = \kappa_i^e + \kappa_i^p \tag{14}$$

$$\epsilon_{ij}^e = \frac{1}{2G}\frac{\partial \tau^2}{\partial \sigma_{ij}}, \quad \kappa_i^e = \frac{1}{2G}\frac{\partial \tau^2}{\partial m_i} \tag{15}$$

$$\epsilon_{ij}^p = \lambda \frac{\partial g}{\partial \sigma_{ij}}, \quad \kappa_i^p = \lambda \frac{\partial g}{\partial m_i} \tag{16}$$

$$\tau^2 = \frac{3}{8}S_{ij}\ S_{ij} + \frac{1}{8}S_{ij}\ S_{ji} + \frac{1}{d_{50}^2}m_i m_i \tag{17}$$

$$f = \tau + \mu(e_0, \gamma^p)p, \quad g = \tau + \beta(e_0, \gamma^p)p \tag{18}$$

where in

τ – second deviatoric stress invariant,

S_{ij} – deviatoric stress $(S_{ij} = \sigma_{ij} - p\delta_{ij})$,

p – mean pressure $\left(p = \frac{1}{3}\sigma_{ii}\right)$,

σ_{ij} – nonsymmetric stress tensor,

m_i – couple stresses,

d_{50} – mean grain diameter,

f, g– yield and potential function,

μ, β– mobilized friction and dilatancy function,

e_0 – initial void ratio,

γ^p – second deviatonic plastic deformation invariant,

ϵ_{ij} – deformations,

κ_i – curvatures (index e denotes elastic and index p plastic deformations),

λ – proportionality factor,

G – shear modulus,

δ_{ij} – Kronecker delta.

The meaning of $f, g, \tau, \gamma^p, \lambda$ in the constitutive relation from Mühlhaus is like in non--polar plasticity (Mróz 1963). The equations $f = 0$ and $g = 0$ describe in the τ, p--plane a yield and a potential curve (Fig. 20). The parameter λ is calculated from the consistency condition $df = 0$. The functions μ, β are connected with angle of internal friction ϕ and the angle of dilatancy ν as follows:
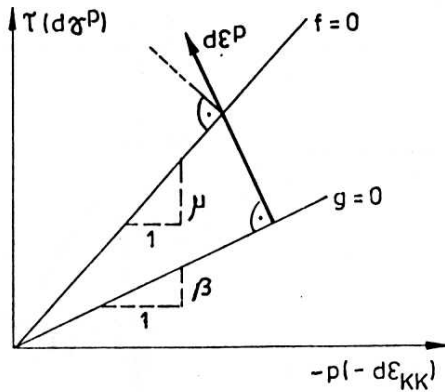
Fig. 20. Yield surface and potential surface in the τ, p-space

$$\mu = \sin \ \phi, \qquad \beta = \sin \ \nu$$

The values of μ and β in the function of void ratio e_0 and plastic distortion γ^p were determined on the basis of the compression tests in a biaxial apparatus. The equation (15) was derived on the basis of consideration of the kinematics (slip and rotation) in a random assembly of circular rods with equal diameter $d = d_{50}$ representing grains, Mühlhaus (1987).

The calculation of the elasto-plastic stiffness matrix is performed in the same way as in the non-polar theory of plasticity. To satisfy full consistency of the yield condition $f = 0$, the trial stress method linearized expansion of the yield condition about trial stress point with the so called „return mapping algorithm" (Ortiz, Simo 1986) was used.

6. Finite element method

6.1. Constitutive parameters

Elastic parameters. The Poisson ratio ν was assumed 0.1. The elastic modules E was assessed according to the Terzaghi formula for the oedometric compression

$$E = \frac{1 + e_o}{C_s} \ \sigma_{22} \tag{19}$$

where e_o denotes the void ratio, C_s the swelling index ($C_s = 0.004$), σ_{22} vertical stress. σ_{22} was calculated with two methods. In the first case, a constant value was assumed $\gamma \cdot h$ (h – length of the pile). In the second case, the varying value with the depth $\gamma \cdot x_2$ was inserted.

Plastic parameters. The calculations were performed only for a dense sand. Fig. 21 shows the adopted curves μ and β ($\phi_p = 38.8°$ for $\gamma^p = 0.5\%$, $\phi_{cr} = 31.2°$, $\nu_p = 19°$). **FE – mesh**. Fig. 22 presents the mesh for the computation (550 triangular elements with linear shape function for an axi–symetric problem were used). The length of the pile was 0.5 m and the diameter was 0.05 m. The mesh was so determined by
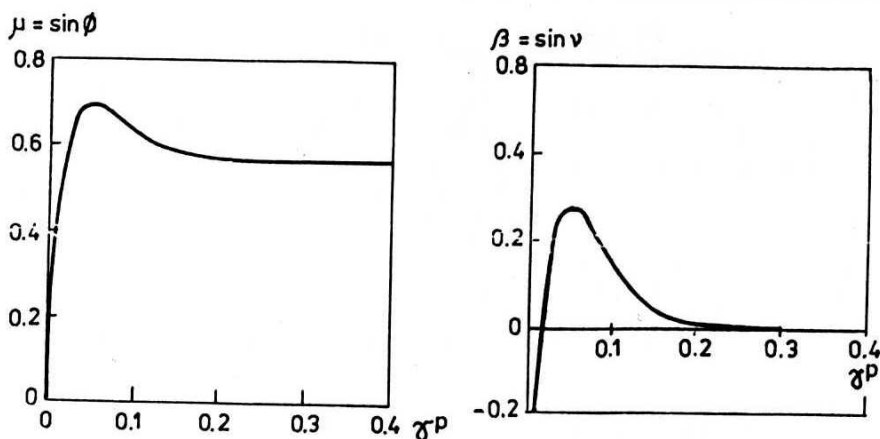
Fig. 21. Friction factor $\mu = f(\gamma p)$ and dilatancy factor
$\beta = f(\gamma p)$ for a dense sand
ϕ – angle of internal friction,
ν – dilatancy angle,
γ^p – plastic distortion

initial calculation that its further refinement has only negligible influence on the pile behaviour. The assumed size of the sand container was big enough and it did not affect the pile forces.

Initial stress state. Our calculations were carried out for two different sets of initial stress conditions (Fig. 23). In the first case, we assumed the intial stress state often used in soil mechanics: K_o – state

$$\sigma_{22} = \gamma \cdot x_2, \tag{20}$$

$$\sigma_{11} = K_o \cdot \sigma_{22} \tag{21}$$

$$\sigma_{33} = \sigma_{11} \tag{22}$$

$$\sigma_{12} = \sigma_{21} = 0 \tag{23}$$

The computation was performed with $K_o = 0.33$.

In the second case, we assumed the initial stresses according to Janssens equation:

$$\sigma_{22} = \frac{0.5 \cdot \gamma \cdot \overline{d}}{4M} \left[1 - \exp\left(-4M \cdot \frac{x_2}{0.5 \cdot d} \right) \right] \tag{24}$$

$$\sigma_{11} = K \cdot \sigma_{22} \tag{25}$$

$$\sigma_{33} = \sigma_{11} \tag{26}$$

$$\sigma_{12} = \sigma_{21} = \sigma_{11} \cdot \tan \varphi_\omega \cdot \frac{(0.25\overline{d} - x_1)}{0.25\overline{d}} \tag{27}$$
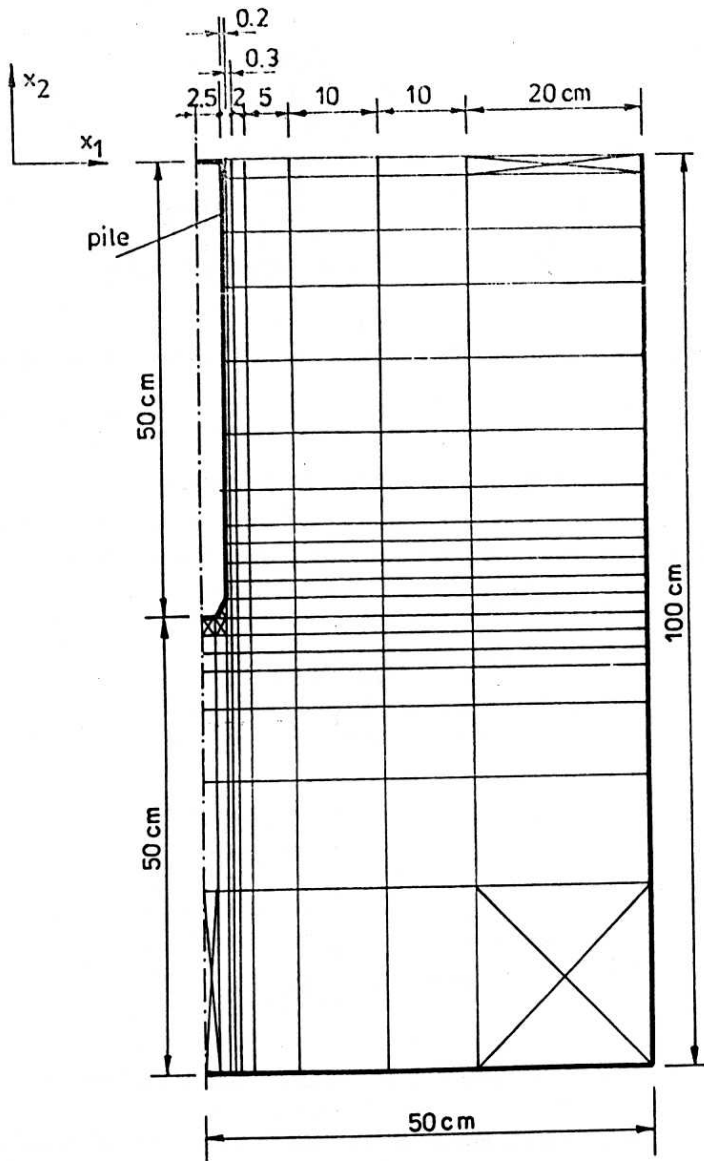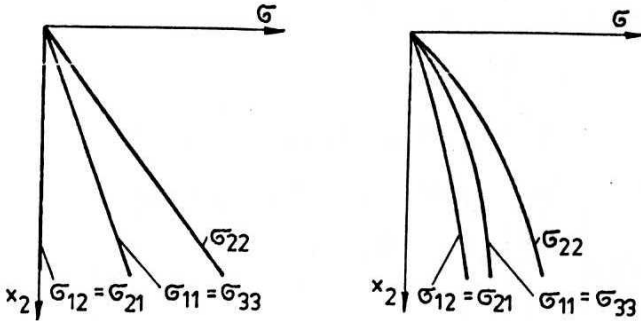
Fig. 22. Mesh of an axi–symmetric boundary value problem

Fig. 23. Initial stress conditions (K_o – stress state and stress state by Janssen)

$$M = K \cdot \tan \varphi_\omega \tag{28}$$

where $\overline{d}$ is the container diameter and φ_ω the wall friction angle.

Boundary conditions. The boundary conditions of an axi-symmetric case are presented in Fig. 24. The assumed boundary conditions along the pile correspond to the
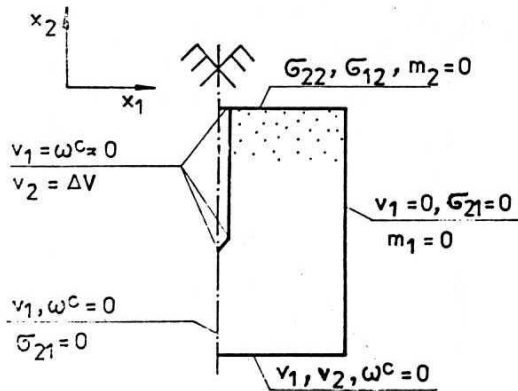

Fig. 24. Boundary conditions of an axi-symmetric problem

very rough surface. The pile was considered as rigid (it means its deformations were not taken into account). The pushing or pulling process was produced numerically by contant successive vertical displacement increment Δv_2 of all nodal point along the shaft and the base of the pile. The diplacement increment $\Delta v_2 = 0.05$ mm was assumed.

Iteration and convergence. A modified Newton-Raphson iteration scheme was carried out with symmetric global stiffness matrix. We applied the initial stress method with a line search, where the initial displacement and rotation increments in every new

displacement step were equal to the increments from the previous displacement step. We adopted the displacement criterion with the following tolerances: $||\Delta v^i||_2 \leq 0.001$ mm and $||\Delta \omega^{c^i}||_2 \leq 0.01$ rad (ΔV^i, $\Delta \omega^{c^i}$ are the incremental displacement and rotation vector in the iteration i and $||\ ||_2$ denotes the Euclidean norm of the vector).

This procedure turned out to give a sufficiently accurate and fast convergence. The magnitude of maximal out-of-balance force $R - F^{i-1}$ at the end of every calculation step was less than 2.5% of the calculated pile shaft force (R denotes the externally applied nodal loads and F is the vector of nodal point forces in the iteration $i - 1$).

7. Numerical results and their evaluation

The following effects on the pile behaviour were investigated.

- pile diameter d,
- grain size d_{50},
- elasticity modulus E,
- dilatancy function β,
- initial stress state.

The length of the pile was assumed constant for all calculations namely $l = 0.5$ m. The Fig. 25-28 show the results obtained from FE-calculation for the pile with $d = 0.05$ m:

- the mantle force Q_m, the point resistance Q_p during pushing in (fig. 25a) and the mantle force Q_m during pulling out dependent on the pile displacement (fig. 25b),
- the sand displacement near the pile (fig. 26, 27),
- the shear stress distribution along the pile mantle (fig. 28).

The force Q_m is equal to the sum of all vertical nodal forces along the pile mantle, the force Q_p is obtained through the multiplication of the pile cross section by the mean vertical stress from the elements under the pile tip. The calculation was carried out for the initial stress state K_o (Eq. 20 – 23 with $K_o = 0.33$), the constant elastic modulus $E = 3300$ kN/m² (Eq. 19 with $\gamma = 17.1$ kN/m³, $e_o = 0.549$, $C_s = 0.004$, $h = 0.5$ m) and the dilatancy function $\beta = 3(\mu - \mu_{cr})$, Fig. 21. The two different mean grain size were considered, namely $d_{50} = 0.24$ mm and $d_{50} = 2.4$ mm. During calculations with $d_{50} = 2.4$ mm, the element breadths in the first three rows at the pile were changed in comparison with the mesh from Fig. 22, that they were not smaller than the grains. These elements were enlarged and assumed corresponding to 0.5, 1.0, 1.0 cm. The breadths of the remaining elements of FE-mesh were not changed. Some conclusions can be drawn from calculations:

- The calculated mantle force during pushing is about 10% bigger than the shaft force during pulling. As compared to the experimental results, the relation between the both forces is too small (in the tests, the force Q_m during pushing was
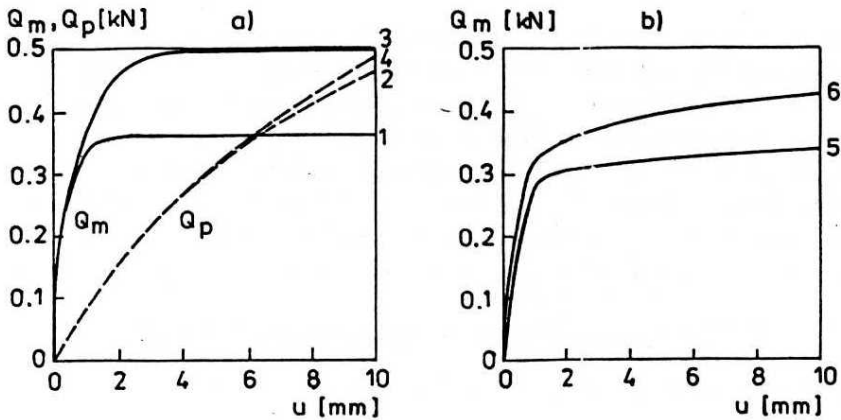
Fig. 25. Calculated shaft force Q_m, base force Q_p during pushing (a) and shaft force Q_m during pulling (b) for vertical pile displacement $u(l = 0.50$ m, $d = 0.05$ m, K_o – initial stress state, $E = 3300$ kN/m^2, $\beta = 3(\mu - \mu_{cr}))$

$$1,5 - Q_m \text{ for } d_{50} = 0.24 \text{ mm}$$
$$2 \quad - Q_s \text{ for } d_{50} = 0.24 \text{ mm}$$
$$3,6 - Q_m \text{ for } d_{50} = 2.4 \text{ mm}$$
$$4 \quad - Q_s \text{ for } d_{50} = 2.4 \text{ mm}$$

two times bigger than the force during pulling). The reason might be, that the initial stress state K_o assumed in the calculation does not correspond to the stress state in the tests. Through the initial pushing of the pile into sand, the K_o – state was disturbed. On the other hand, the same dilatancy angle and the same angle of internal friction were assumed to the calculations for pushing and pulling. The triaxial tests for sand show, that the both angles are for compression (this test might correspond approximately to the pile pushing) some degrees bigger than for extension (this test might correspond approximately to the pile pulling). The bigger the both angles, the greater the bearing capacity of piles. Therefore the bigger mantle force could occur during pushing than during pulling.

- The calculated maximal mantle force for pulling is in accordance with the experimental results.

- The mantle force Q_m reaches the limit value (for pushing) or the first clear maximum (for pulling) for $u/d = 4 - 6\%$. The base force Q_p increases on the other hand clear in the range of the displacements $u = 0 - 1.0$ cm.

- The 10-times increase of mean grain causes the increase of the force Q_m during pushing about 40% and during pulling about 30%. This result confirms, that the force values from model experiments are not comparable with the values from big experiments. The mantle force from model experiments is overestimated because of the scale effect, which is caused by the dilatancy constraint of sand in the shear zone along the pile shaft. The dilatancy is constrainted by the mass of the surrounding soil. The results from model experiments can be then transfered to
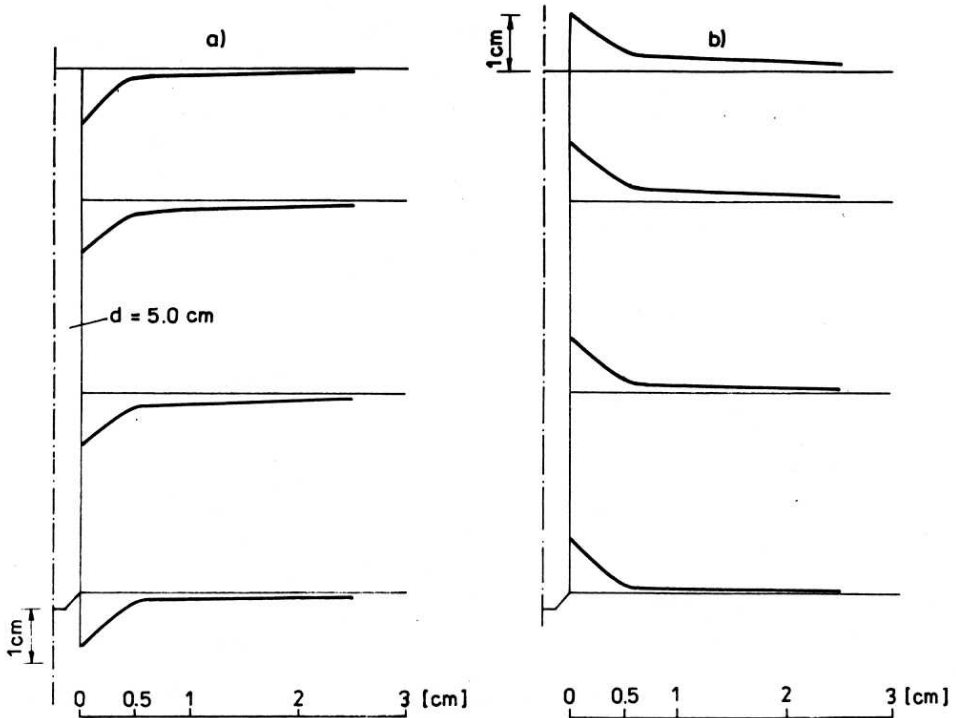
Fig. 26. Calculated displacements along the pile ($l = 0.5$ m, $d = 0.05$ m,
$d_{50} = 0.24$ mm)   a) during pushing   b) during pulling

the big piles if the ratio between grain size and pile dimension is the same in the
both cases.

- The size of the sand grains has almost no influence on the base force. The force
  Q_p is for $d_{50} = 2.4$ mm only about $1 - 2\%$ bigger than for $D_{50} = 0.24$ mm.
- The calculated thickness of the shear zone along the pile shaft, which does not
  depend on the FE-mesh amounts approximately to $20 \cdot d_{50}$ for $d_{50} = 0.24$ mm to
  $7 \cdot d_{50}$ for $d_{50} = 2.4$ mm (Fig. 26, 27).
- The distribution of the calculated shear stresses in the residual state (big displa-
  cement) has the triangle form during pulling and approximately the rectangle
  from (except upper pile region) during pushing (Fig. 28). The stresses have a
  tendency to oscillate with travelling peaks.
- The earth pressure coefficients (relation between radial and vertical stresses)
  along the pile shaft are equal 1 in the residual state.

The Figures 29-31 present the influence of the pile diameter d on the forces Q_m
and Q_p. The normalized mantle force $Q_m/\gamma l d^2$ and the normalized base force $Q_p/\gamma d^3$
in function of u/d are given.

- The mean shear stress along the pile shaft $\bar{\tau}_m = Q_m/\pi d l$ and the mean point
  stress $\bar{\sigma}_p = Q_p/0.25\pi d^2$ decrease for increasing pile diamters. The stress $\bar{\tau}_m$ is: for
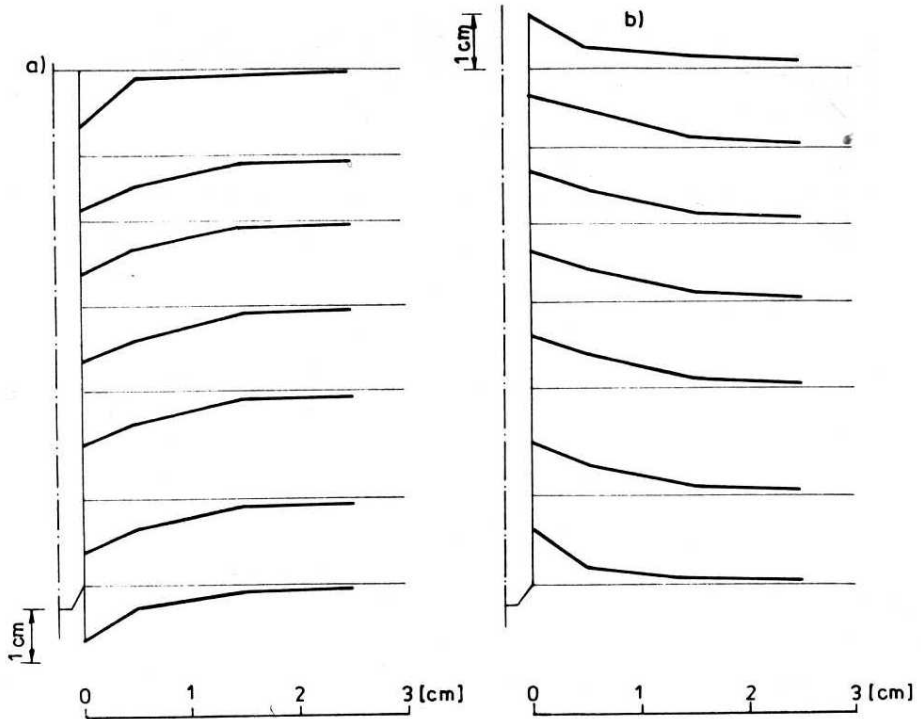
Fig. 27. Calculated displacements along the pile ($l = 0.5$ m, $d = 0.05$ m,
$d_{50} = 2.4$ mm)   a) during pushing   b) during pulling

the pile with $d = 0.15$ m, independent of the grain size, about 30% smaller than
for the pile with $d = 0.05$ m, and the stress σ_p is corresponding smaller about
40%.

- The forces Q_m reach maximal values for similar big displacements of the pile with
  $d = 0.15$ m as in the case of the pile with the smaller diameter.

In Fig. 32 are presented the calculations of Q_m and Q_p for the pile during pushing
with the smaller dilatancy angle ($\beta = 2(\mu - \mu_{cr})$, $\nu_p = 12.5°$) and in Fig. 33 with the
5-times bigger elasticity modulus ($E = 16500$ kN/m²).

- The assumption of the dilatancy function smaller about 33% causes the decrease
  of Q_m about 30% and of Q_p about 35%.
- Owing to the 5-times increase of E-modulus, the calculated mantle force is 2.5-
  -times and the base force 3-times bigger. The values of Q_m and Q_p for $E = 16500$
  kN/m² are in a good agreement with experimental results.
- The influence of E and β on the mantle force during pulling is quantitatively
  similar as during pushing.

The results from Fig. 34, 35 were obtained with the elasticity modulus varying with
the depth according to the Eq. 19 ($E = 6600 \cdot x_2$ kN/m³). Some conclusions:
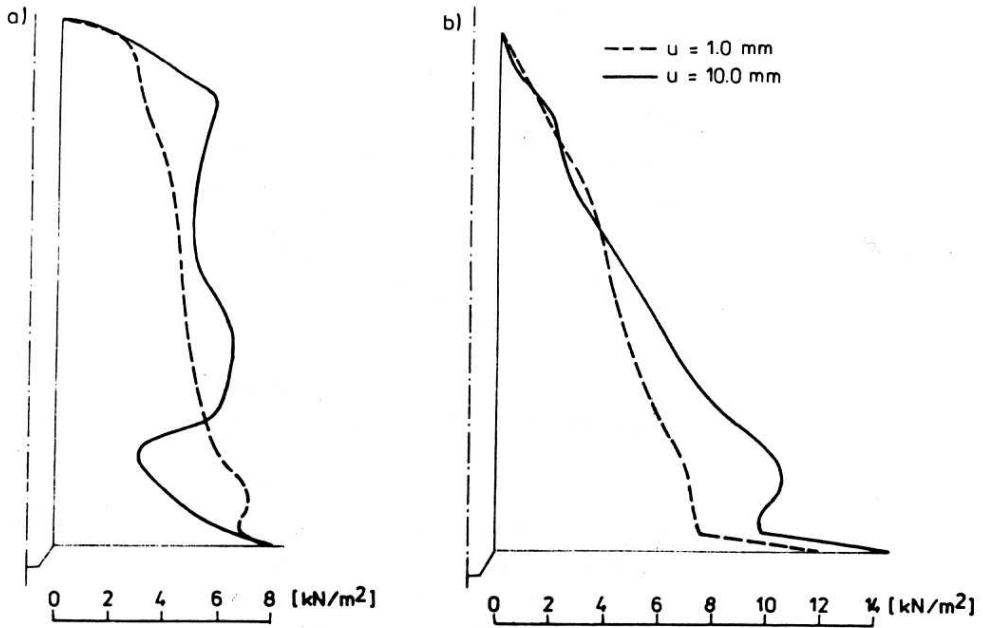
Fig. 28. Calculated shear stress distribution along the pile for two different pile displacements u
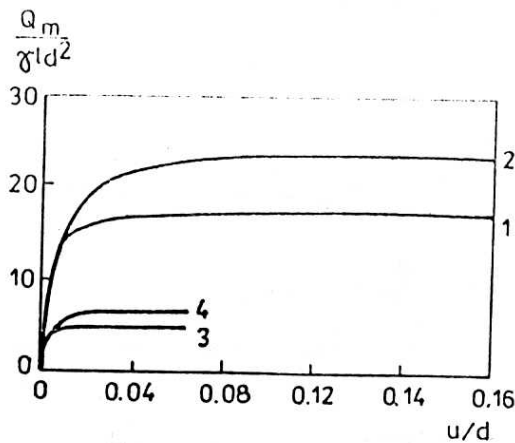
a) during pushing   b) during pulling

Fig. 29. Calculated normalized shaft force Q_m during pushing (K_o – initial stress state, $E = 3300$ kN/m^2, $\beta = 3(\mu - \mu_{cr})$)

$1 - d = 0.05$ m, $d_{50} = 0.24$ mm
$2 - d = 0.05$ m, $d_{50} = 2.4$ mm
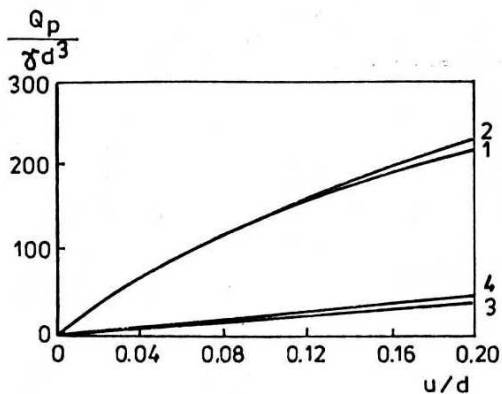$3 - d = 0.15$ m, $d_{50} = 0.24$ mm
$4 - d = 0.15$ m, $d_{50} = 2.4$ mm

Fig. 30. Calculated normalized shaft force Q_p during pushing (K_o – initial stress
state, $E = 3300$ kN/m^2, $\beta = 3(\mu - \mu_{cr})$)

$1 - d = 0.05$ m, $d_{50} = 0.24$ mm
$2 - d = 0.05$ m, $d_{50} = 2.4$ mm
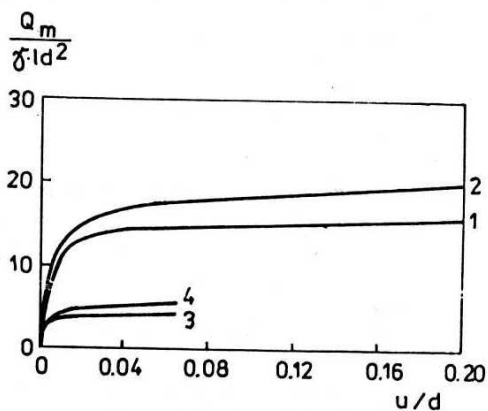$3 - d = 0.15$ m, $d_{50} = 0.24$ mm
$4 - d = 0.15$ m, $d_{50} = 2.4$ mm

Fig. 31. Calculated normalized shaft force Q_m during pulling (K_o – initial stress
state, $E = 3300$ kN/m^2, $\beta = 3(\mu - \mu_{cr})$)

$1 - d = 0.05$ m, $d_{50} = 0.24$ mm
$2 - d = 0.05$ m, $d_{50} = 2.4$ mm
$3 - d = 0.15$ m, $d_{50} = 0.24$ mm
$4 - d = 0.15$ m, $d_{50} = 2.4$ mm

Fig. 32. Calculated shaft force Q_m and point force Q_p during pushing for vertical pile displacements u ($l = 0.5$ m, $d = 0.05$ m, $d_{50} = 0.24$ mm, K_o – initial stress state, $E = 3300$ kN/m^2, $\beta = 2(\mu - \mu_{cr})$)
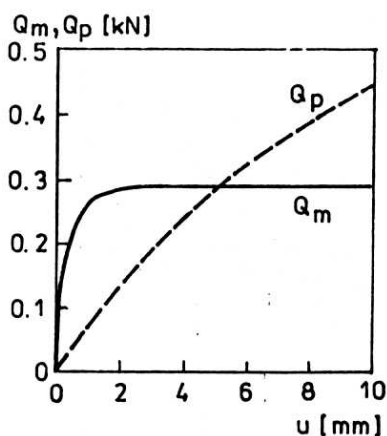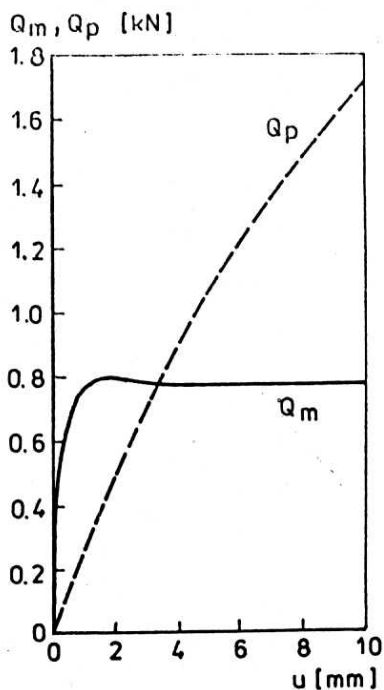

Fig. 33. Calculated shaft force Q_m and point force during pushing for vertical pile displacements u ($l = 0.5$ m, $d = 0.05$ m, $d_{50} = 0.24$ mm, K_o – initial stress state, $E = 16500$ kN/m^2, $\beta = 3(\mu - \mu_{cr})$)
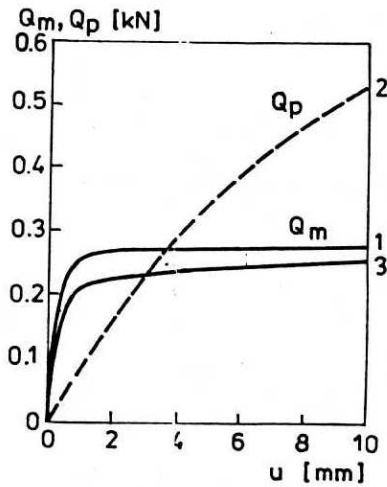
Fig. 34. Calculated shaft force Q_m, base force Q_p during pushing and shaft force Q_m during pulling for the pile displacementu u ($l = 0.5$ m, $d = 0.05$ m $D_{50} = 0.24$ mm K_o – initial stress state, $E = 6600 \cdot x_2$ kN/m^3, $\beta = 3(\mu - \mu_{cr})$)

1 – Q_m during pushing
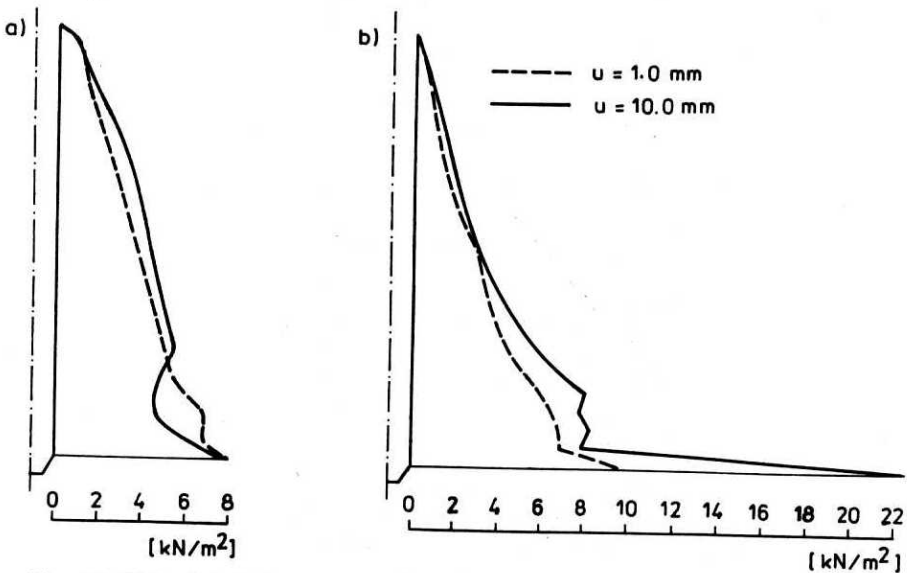2 – Q_p during pushing
3 – Q_m during pulling

Fig. 35. Calculated shear stress distribution along the pile for two different pile displacements a) during pushing b) during pulling
($l = 0.5$ m, $d = 0.05$ m, $d_{50} = 0.24$ mm, K_o – initial stress state, $E = 6600 \cdot x_2$ kN/m^2, $\beta = 3(\mu - \mu_{cr})$)

– The values of Q_m and Q_p in the function of u are qualitatively the same as in the case of calculations with the constant E – modulus.

– The distribution of shear stress along the pile shaft during pushing is qualitatively similar as during pulling (triangular form) in contrast to the rectrangular distribution which was obtained with the constant elasticity modulus for big pile displacements (Fig. 28).

In Fig. 36 are presented the results of Q_m and Q_p for the initial stress state according to Janssen (Eq. 24 – 28 with $M = 0.3$ and $\varphi_w = 0.9 \ \phi_p$). This stress state was only
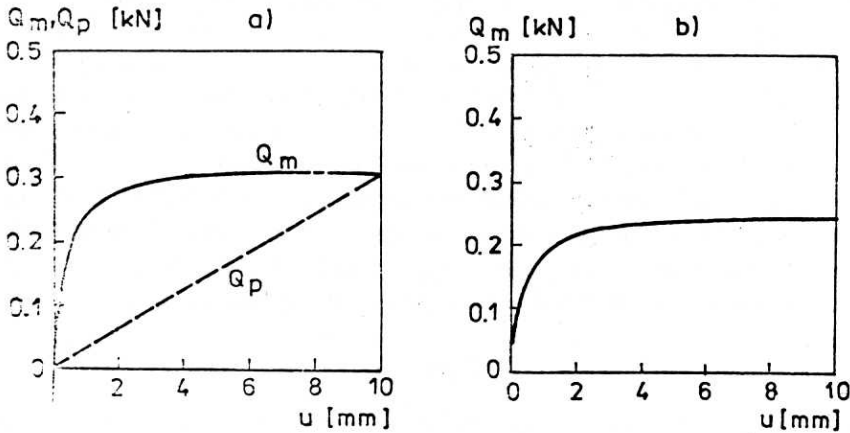

Fig. 36. Calculated shaft force Q_m, base force Q_p during pushing (a) and shaft force Q_m during pulling (b) for vertical pile displacement u
($l = 0.5$ m, $d = 0.05$ m, $d_{50} = 0.24$ mm, initial stress state by Janssen, $E = 3300$ kN/m^2, $\beta = 3(\mu - \mu_{cr})$)

assumed in the region between the pile and container wall ($x_2 = 0 - 0.5$ m). Below the pile, this state changed into the K_o – state. The computation was performed for $E = 3300$ kN/m^2. The consideration of shear stresses at the beginning of the pile load causes, that the maximal forces Q_m, Q_p are about 20% smaller than with the assumption of the K_o – state in the whole sand container. The kind of the initial stress state in sand along the pile has thus an effect on the results.

8. Conlusions

The numerical results show that the Cosserat approach in connection with a finite element method is very usefull to study pile problems in regard to:

- investigation of the scale effects,
- determination of the influence of the pile diameter and grain diameter on the pile forces,
- determination of the thickness of the shear zone along the pile.

The usefulness of the constitutive relation from Mühlhaus for studying the pile bearing capacity is similar as all elasto–plastic constitutve relations limited because the results of the shaft and base forces depend on the magnitude of the elasticity modulus assumed in the calculations. The determination of the realistic elasticity modulus for pile problems by means of triaxial and biaxial tests is very difficult. Sand does not produce pure elastic behaviour and the E-modulus depends strongly on the stress level. For the determination the pile bearing capacity, the E-modulus should be fitted with the aid of the back calculations on the basis of the experimental results. With the elasticity modulus determined in this way, the bearing capacity of the piles with the different dimensions could be described realistically with elasto-plastic constitutive relation.

References

Gwizdała K., (1977), *Bearing capacity of large diameter bored piles*, (in Polish), Doctor's dissertation, Technical University of Gdańsk.

Günther W., (1958), *Zur Statik und Kinematik des Cosserat'schen Kontinuums*, Abh. Braunschweigische Wiss., Band 10.

Kerisel L., (1962), *Foudations profondes*, Annales de l'Inst. Techn. du Batim. et das Travaux, no. 179, Paris.

Mindlin R.D., (1969), *Micro-structure in Linear Elasticity*, Archives for Rat. Mech. and Anal. 16.

Mühlhaus H.B., (1987), *Berücksichtigung von Inhomogenitäten im Gebirge im Rahmen einer Kontinuumstheorie*, Habilitation. University Karlsruhe, West Germany.

Mróz Z., (1963), *Nonassociated Flow Laws in Plasticity*, Journal de Mechanique 1.

Ortiz M., Simo J.C., (1986), *An Analysis of a New Class of Integration Algorithms for Elastoplastic Constitutive Relation*, Int. Jour. for Num. and Analit. Mech. in Geomech., Vol. 23.

Schäfer H., (1967), *Das Cosserat Kontinuum*, Zeitschrift für Angewandte Mathematik und mechanik, Band 17, Heft 8.

Spang J., (1972), *Die Bestimmung der Tragfähigkeit von Grossbohrphälen*, Strassen und Tiefbau, H. 5.

Tejchman A., (1966), *Distribution of total load into point and shaft resistance (in Polish)*, Archivum Hydrotechniki, No. 1.

Tejchman A., (1966), *Comparison between shaft resistance for compression and tension piles (in Polish)*, Archivum Hydrotechniki, no. 2.

Tejchman A., (1971), *Skin friction and point resistance of a model pile in sand*, Bulletin No. 29, Danish Geotechnical Institute, Copenhagen.

Tejchman A., (1973), *Earth pressure state around pile model in pushing and pulling (in Polish)*, Archivum Hydrotechniki, No. 3.

Tejchman A., Gwizdała K., (1979), *Analysis of safety factors of bearing capacity for large diameter piles*, Proc. of the 7 the European Conference on SMFE, Brighton.

Tejchman A., (1988), *Study on scale effect in pile models*, Karlsruhe University, (non published).

Tejchman J., (1989), *Scherzonenbildung und Verspannungseffekte in Granulaten unter Berücksichtigung von Korndrehungen*, Dissertation, University Karlsruhe, West Germany.

Wernick E., (1978), *Tragfähigkeit zylindrischer Anker in Sand unter besonderer Berücksicchtigung des Dilatanzverhaltens*, Veröffentlichungen des Institutes für Bodenmechanik und Felsmechanik der Universität in Karlsruhe, Heft 75.

Summary

The behaviour of model and full scale piles in a granular soil under vertical load was investigated. Some model tests results were compared with numerical calculations by means of a finite element method using constitutive law by Mühlhaus. An elasto--plastic constitutive relation by Mühlhaus with hardening and softening was laid down for granular bodies in the frame of a nonpolar continuum (Cosserat continuum). Each material point in a nonpolar continuum has, for a plane and axi-symmetric case, three degrees of freedom (the two displacements and the rotation independent of the displacements). The consitutive law differs from the usual theory of plasticity due to the presence of the couple stresses and the mean grain diameter. The numerical results show that the method used is very useful for studing the scale effect and the shear zone thickness along the pile. It is also suitable to investigate the bearing capacity of piles when realistic elastic soil parameters are used.

Streszczenie

W pracy przedstawiono wyniki badań zachowania się pali modelowych i pali o naturalnej wielkości w piasku pod obciążeniem pionowym. Niektóre z tych wyników zostały porównane z wynikami numerycznymi w oparciu o metodę elementów skończonych i prawo konstytutywne Mühlhausa. Sprężysto-plastyczne prawo konstytutywne Mühlhausa ze wzmocnieniem i osłabieniem, zostało sformułowane w ramach mechaniki ośrodka ciągłego Cosserat.

Każdy materialny punkt tego ośrodka ma dla przypadku płaskiego i osiowo-symetrycznego trzy stopnie swobody (dwa przemieszczenia i niezależny od nich obrót). Prawo konstytutywne różni się od praw klasycznej teorii plastyczności obecnością momentów naprężeniowych i średniej średnicy ziarna. Wyniki numeryczne pokazują przydatność zastosowanej metody do obliczania efektu skali uwzględniającego średnice pala i ziarn gruntu oraz szerokości strefy ścinania wzdłuż pobocznicy pali. Metoda ta może być także przydatna do obliczania nośności pali pod warunkiem przyjęcia wiarygodnych wielkości sprężystych ośrodka gruntowego.